Inductive sensor design for electromagnetic tracking in image guided interventions

Marco Cavaliere, Oisín McVeigh, H. Alexander Jaeger, Stephen Hinds, Kilian O'Donoghue and Pádraig Cantillon-Murphy

***Abstract*— As the importance and prevalence of electromagnetic tracking in medical and industrial applications increases, the need for customized sensor design has escalated. This work focuses on AC-based electromagnetic tracking systems where off-the-shelf inductive sensors may not be optimal for many medical instruments or tracking applications. We present a repeatable approach for the design, optimisation and implementation of air-core and ferrite-core inductive sensors suitable for AC-based electromagnetic tracking. Coil-based sensors were designed and tested to investigate the effect of the usual coil parameters such as turn count, geometry and core material on sensor tracking accuracy and precision. Our methodologies were experimentally validated using the Anser EMT system which enabled rapid experimental deployment. Experimental performance is reported compared to off-the-shelf sensors. Static tracking errors of less than 2mm were achieved and close correlation with theoretical design sensitivity and precision was observed. This work may represent a valuable tool in the design of bespoke sensors for electromagnetic tracking where customize sensitivity and form factor are critical.**

***Index Terms*— Electromagnetic tracking, image guidance, laparoscopy, navigation, robotic surgery, sensors, tracking**

I. Introduction

ELECTROMAGNETIC tracking (EMT) is the gold standard technology for tracking and navigation in image-guided interventions when there is no line of sight to the target. Clinical applications which currently exploit EMT for virtual navigation include bronchoscopy [1] [2], neurosurgery [3] and ear, nose and throat surgery [4]. Commercial systems which use EMT for navigation include the Medtronic superDimension [5], the Veran SPiN system [6] and the Fiagon system [7]. EMT is also increasingly common in visualization systems used for surgical simulation and robotic surgery. A number of OEM EMT systems have been developed and are suitable for third-party use and research purposes. These include the NDI Aurora (*Northern Digital Inc., Waterloo, Canada*), the NDI Trakstar (*Northern Digital Inc., Waterloo, Canada*, formerly sold by *Ascension Technologies*) and the Polhemus Fastrak (*Polhemus Inc., Colchester, Vermont*).

To date, EMT sensors, such as those shown in Figure 1, are commercially manufactured to specified sensitivities in fixed geometries. However, with the increasing prevalence of EMT across image-guided interventions, the need for different sensor geometries and sensitivities has become more important. While customized sensor design is not feasible with proprietary systems, the Anser EMT system [8] facilitates new sensor geometries designed for specific applications, such as laparoscopic instruments and endoscope tracking.

In this work, large-area coils are designed, manufactured and integrated for use in Anser EMT. The goal of this work is to demonstrate the feasibility of the bespoke inductive sensor design for electromagnetic tracking systems. Variations in sensor accuracy with turn count and coil area are investigated, using both air and ferrite core geometries. A possible application is proposed in Figure 2, where a coil is wound around the shaft of an instrument, such as a bronchoscope or laparoscopic instrument, to facilitate tracking during image-guided interventions.

The work represents the first attempt to characterize large-diameter inductive sensors and demonstrate their integration with electromagnetic tracking systems. The results offer valuable guidelines for the choice of sensor parameters in customized design, within the limits of hand-wound geometries and 5 degree of freedom (5 DoF) sensing.

II. Electromagnetic Tracking

Almost all commercial EMT systems typically used in clinical applications are based on the principle of electromagnetic induction (Faraday's law), even if other techniques are possible, such as the pulsed DC field of NDI Trakstar. Faraday's law is given by Equation 1, where v_s is the induced voltage in Volts and Φ is the sensor magnetic flux in Webers:

$$v_s(t) = -\frac{d\Phi(t)}{dt} \tag{1}$$

Manuscript received Month xx, 2xxx; revised Month xx, xxxx; accepted Month x, xxxx. This work is supported by Science Foundation Ireland Technology Innovation and Development Award TIDA17/4897 and by the Eureka Eurostars project number 11581, entitled 'Mariana: Image-guided catheter navigation in the outer airways'.

M. Cavaliere is with the School of Engineering, University College Cork and the Tyndall National Institute, Dyke Parade, Cork, Ireland (e-mail: m.cavaliere.ucc@gmail.com).

O. McVeigh and S. Hinds are with the School of Engineering, University College Cork.

K. O'Donoghue is with the Tyndall National Institute, Dyke Parade, Cork, Ireland.

H. A. Jaeger is with the School of Engineering, University College Cork, Cork, Ireland (e-mail: h.jaeger@umail.ucc.ie).

P. Cantillon-Murphy is with the School of Engineering, University College Cork and the Tyndall National Institute, Dyke Parade, Cork, Ireland (e-mail: p.cantillonmurphy@ucc.ie).

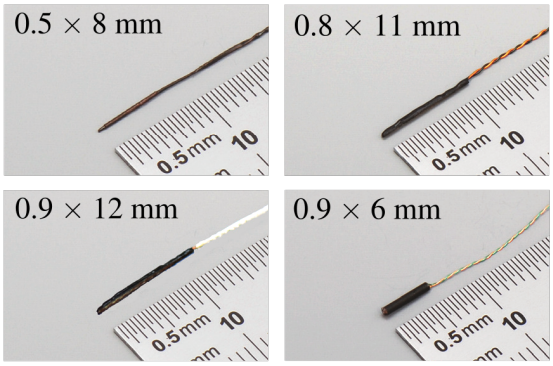

Fig. 1. Commercially available EMT sensors are characterized by tiny diameters of less than 1 $\mathbf{mm}$. Ferrite cores are necessary to get a sensitivity in the range of $\mathbf{0.1-0.2\,V\,T^{-1}\,Hz^{-1}}$. The main drawbacks are high cost, high fragility, non-linearity introduced by the ferrite core.

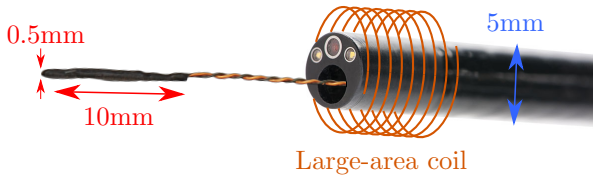

Fig. 2. In some applications, the addition of a large-area sensor could facilitate the tracking procedure, by providing extra information on position and roll angle. As demonstrated in this work, large-area sensors are characterised by high sensitivity even in the absence of a ferrite core.

AC-based EMT systems tend to be more amenable to smaller sensor design, which might address shortcomings in current systems such as electromagnetic distortion, proprietary interfaces and relatively high hardware costs. Recent efforts to design open-source EMT architectures [9] [10] also rely on tiny sensors, but are open to work with bigger sensors, such the ones presented in this work.

For a coil-based inductive sensor of cross-sectional area A_c and with N turns, Equation 1 is more specifically given by Equation 2, in terms of magnetic flux density $\mathbf{B}$ experienced by the sensor:

$$v_s(t) = -N\frac{d}{dt}\oint_{A_c} \mathbf{B}\cdot\mathbf{n}\,dA \tag{2}$$

where $\mathbf{n}$ is the unit vector normal to the coil cross-sectional area A_c.

In EMT systems which use single-axis sensors, $\mathbf{B}$ is typically provided by a planar transmitter board and it is spatially and temporally varying, with a number of unique frequency components which can be used to resolve the sensor position and orientation in the working volume around the transmitter board. For small sensors, such as those shown in Figure 1, the variation in flux density across the sensor cross-section is usually small, so that Equation 2 may be simplified to Equation 3:

$$v_s(t) = -N\frac{d\mathbf{B}}{dt}\cdot\mathbf{n}\,A_c \tag{3}$$

If d_i and d_o are the innermost and the outermost winding diameters respectively, A_c is given by Equation 4 or, considering the average winding diameter, can be approximated by Equation 5:

$$A_c = \frac{1}{d_o-d_i}\int_{d_i}^{d_o}\frac{\pi}{4}x^2\,dx = \frac{\pi}{12}(d_i^2+d_id_o+d_o^2) \tag{4}$$

$$\simeq \frac{\pi}{4}\left(\frac{d_i+d_o}{2}\right)^2 \tag{5}$$

The addition of a ferromagnetic core can significantly increase the received sensor voltage v_s, particularly in the case of smaller sensor geometries (Figure 1). The high-permeability material tends to concentrate the magnetic flux lines and to increase the local B field. The magnetic flux through the coil area depends on the ferrite core relative permeability μ_r and on the geometry of the sensor. Demagnetisation can occur where in shorter cores some magnetic flux lines can find a closed path inside the core itself, which has low reluctance, adding a negative contribution to the flux linked to the coil. The parameter μ_a is defined as *apparent magnetic permeability* of the core and accounts for this phenomenon.

The ferromagnetic core can dramatically increase the sensitivity of the sensor, but this comes at the cost of linearity. All ferromagnetic materials are inherently non-linear in nature, hence the output of the sensor will exhibit some non-linear behaviour, which can depend on many factors, such as frequency, temperature, field strength etc. [11]. Increased noise is also observed from ferromagnetic materials due to Barkhausen effect [12].

Considering the possible presence of a ferromagnetic core, the sensor output voltage is then:

$$v_s(t) = -\mu_a N\frac{d\mathbf{B}}{dt}\cdot\mathbf{n}\,A_c \tag{6}$$

where $\mu_a = 1$ in the case of air-core coils and $\mu_a > 1$ in the presence of a ferrite core.

If the magnetic field applied to the sensor is sinusoidal with amplitude $\mathbf{B_0}$ (Equation 7), as is typically the case for EMT systems, Equation 6 can be further simplified into Equation 8, where ω is the received field angular frequency:

$$\mathbf{B} = \mathbf{B_0}(x,y,z)\,\sin\omega t \tag{7}$$

$$v_s(t) = -\mu_a N\omega\cos\omega t\,\mathbf{B_0}\cdot\mathbf{n}\,A_c \tag{8}$$

If only the magnitudes are considered (capital letters V_s and B_0) and the field is perpendicular to the area, the dependence on the magnetic induction may be made explicit and Equation 9 is obtained, where f is the frequency in Hertz and k_s is the sensitivity of the sensor in Volts per Tesla per Hertz ($\mathrm{V\,T^{-1}\,Hz^{-1}}$):

$$V_s = \mu_a N 2\pi f\,B_0\,A_c = k_s f B_0 \tag{9}$$

$$k_s = 2\pi N A_c \mu_a \tag{10}$$

Typical values for the sensitivities of commercial sensors, such as the one designed for use with the Aurora Tracking System, are $0.1-0.2\,\mathrm{V\,T^{-1}\,Hz^{-1}}$ [13, Chap. 3].

Large-area sensors, like the ones presented in this work, are ideal for designing and testing EMT systems for instrument tracking in image-guided interventions. Non-linearities can be

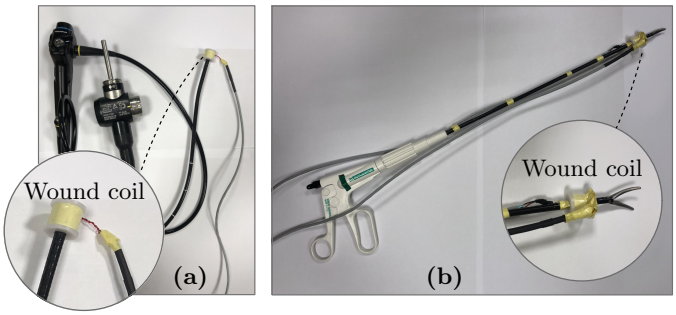

Fig. 3. Large-diameter coils like the ones studied in this work can be used for medical instrument tracking, such as **(a)** in bronchoscopy or **(b)** for laparoscopic graspers.

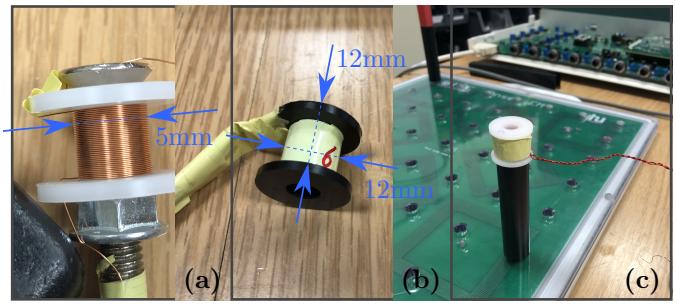

Fig. 4. **(a)** Enamelled copper wire wound on the Delrin coil former. **(b)** Each completed winding layer was secured with magnet tape. Also shown is the removable ferrite core. The core may be inserted into the former lumen. **(c)** The wound coil is located above the Anser EMT calibration board using the Delrin former during calibration and testing.

avoided by using air-core coils with acceptable sensitivities, where larger area A_c compensates for smaller μ_a in Equation 10. Bespoke sensor coils are simpler to manufacture and less costly to produce at production volumes.

Many guided medical procedures can take advantage of such coils. Figure 3 demonstrates prototype coil integration with commonly used instruments such as a bronchoscope and a laparoscopic grasper. EMT is the only means of tracking the end effectors of these instruments during procedures where surgical line of sight cannot be maintained.

For large sensors, the single-point approximation of Equation 3 does not hold. Nevertheless, positional error smaller than the coil radius can be achieved by the use of more general Equation 2.

III. Materials and Methods

A. Sensor Design

The main design parameters for consideration are the sensor sensitivity and frequency range of operation. AC magnetic fields used in EMT operate under 100 kHz. Higher frequencies are attenuated by human tissue and are susceptible to modelling error due to eddy currents induced in conductive instruments that naturally populate the clinical space.

This work focuses on the physical design of coils for EMT. Design parameters such as turn count, cross-sectional area and core material are investigated and their effects on tracking accuracy analysed.

Five inductive sensors were wound on custom Delrin formers. The parameters are summarized in Table I, where N is the turn count, l_c is the coil length, d_i and d_o are respectively the inner and outer coil diameters, referred to the innermost and the outermost winding, and d_w is the wire diameter.

Considering a coil with an average diameter of 10 mm, a sensitivity k_s of $0.15\,\mathrm{V\,T^{-1}\,Hz^{-1}}$ is obtained with about 300 turns. With Coil A as a baseline, Coil B increases the average area, while Coils C, D and E change the number of turns. The characterisation of Coil B over frequency was also performed with the insertion of a ferrite core. The static accuracy of Coils C, D and E was also tested with a ferrite core. The aim is to investigate how the parameters N, A_c and μ_a affect the sensor sensitivity and verify the simplifications of Equation 10.

Each coil was carefully hand-wound, with visual inspection and photography used to confirm turn count upon completion

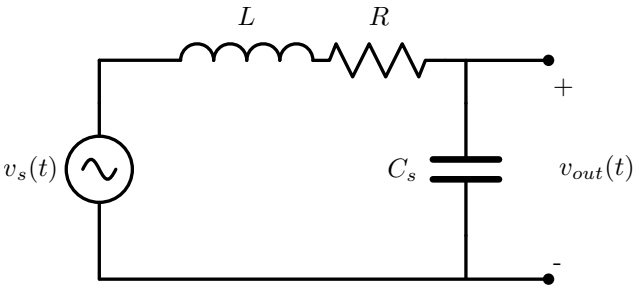

Fig. 5. Lumped parameters circuit for an inductive sensor. $\boldsymbol{v_s}$ is the field induced voltage, $\boldsymbol{L}$ and $\boldsymbol{R}$ are the sensor series inductance and resistance respectively and the shunt capacitor $\boldsymbol{C_s}$ accounts for the parasitic capacitance effects.

of each layer. A typical completed winding layer is shown in Figure 4a. One turn of magnet tape was used to fix each layer upon winding, as shown in Figure 4b. Each former could facilitate the insertion of a ferrite rod core, also shown in Figure 4b. The final wound sensor coil was terminated with a twisted-pair cable (Figure 4c). Ferrite cylinders were investigated as magnetic cores. They measured 12 mm in length and 6 mm in diameter and were made of 3C90 grade ferrite (*Ferroxcube, Eindhoven, The Netherlands*), with a relative permeability of $\mu_r = 2300$.

B. Characterisation over frequency

An inductive magnetic sensor can be modelled as the series of many distributed inductances and resistances, with parasitic capacitances between the turns [14]. The lumped parameters circuit, valid from low frequency to the first self-resonance frequency (SRF), is an $L-R$ series with a shunt capacitor C_s, as in Figure 5. Considering Equation 9, the output voltage of the sensor is given by Equation 11, with $\omega = 2\pi f$:

$$V_{out} = \frac{k_s f B}{1 - \omega^2 LC + j\omega RC} \tag{11}$$

While sensitivity is easily predicted by Equation 10, the linear range of operation of the inductive sensor depends on its inductance and parasitic capacitances, for which there are not general and accurate analytical formulas and simulation tools might be involved. Frequency response was experimentally calculated. The purpose is to validate Equation 10 for sensitivity and the lumped circuit model of Figure 5, as well

Coil	N	l_c [mm]	d_i [mm]	d_o [mm]	d_w [mm]	A_c [mm^2]	R [Ω] (in DC)	L [μH] (air core)
A	321	12	9	12.5	0.19	90.76	7.4	604
B	319	12	11	14.1	0.19	123.70	8.6	804
C	120	12	9	12.2	0.32	88.25	0.8	91
D	216	12	9	11.4	0.19	81.71	9.4	425
E	417	12	9	12.0	0.15	86.59	14.3	1018

TABLE I

PROPERTIES OF EMT SENSOR COILS DESIGNED AND TESTED IN THIS WORK. $\boldsymbol{R}$ AND $\boldsymbol{L}$ ARE THE RESULTING SENSOR RESISTANCE AND INDUCTANCE RESPECTIVELY.

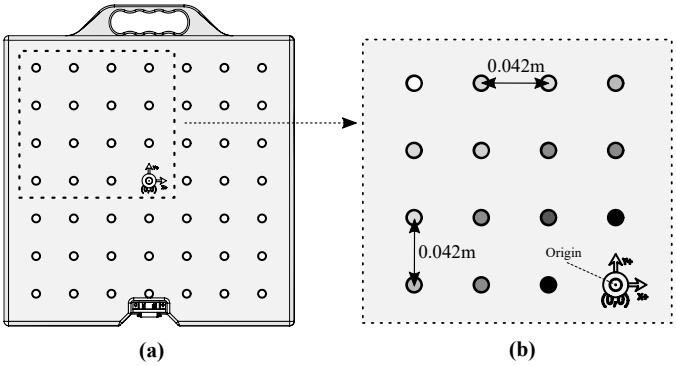

Fig. 6. **(a)** Top-down view of Anser EMT field generator showing the 49 positions used for calibration and static position accuracy testing. **(b)** Zoomed in section of the top-left quadrant of the field generator. Positions are shaded according to their (x, y, z) Euclidean distance from the origin $(0, 0, 0)$.

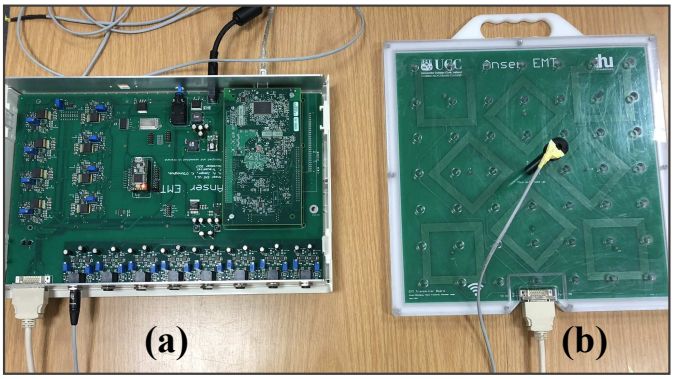

Fig. 7. **(a)** Anser EMT base station and **(b)** field generator used in experiments. The board contains eight field-generating coils below a 49-points grid of equispaced holes. In the experiments, the coils were inserted into the holes using two heights Delrin formers, for a total of 98 position measurements per coil.

as to demonstrate that the coils presented in this work show SRF much higher than the frequency range of interest for EMT applications.

The five coils of Table I were tested using a customized Helmholtz coil. For a frequency range from 1 kHz to 1 MHz, the analytically known [15] magnetic field produced by the Helmholtz coil was compared to the output voltage measured.

The measurements were fitted in a least-squares sense over low frequency for $|V_{out}| \approx |V_s| = k_s f |B|$, to determine the value of the sensitivity k_s. With reference to Figure 5, R and L were measured with an impedance analyser (4284A Precision LCR Meter, *Keysight Technologies, Santa Rosa, California*), the SRF, f_0, was identified by the maximum output voltage of the measured points and C_s was consequently defined by Equation 12:

$$C_s = \frac{1}{(2\pi f_0)^2 L} \tag{12}$$

C. Static Accuracy Testing

The sensor model can introduce a positional error as large as the sensor radius when single point approximation is considered. To achieve a better spatial resolution, Equation 2 was numerically evaluated to perform the following magnetic tracking procedures.

Each sensor was calibrated for use with the Anser EMT system, using the previously reported model-fitting routine [10]. This involves a 7×7 point-by-point calibration of the sensor and the Anser field generator, shown in Figure 6. For 5 DoF sensors calibration, the coil is positioned at a fixed distance and orientation (z-oriented) relative to the transmitter, as shown in Figure 7.

The measured sensor magnetic flux at each point is compared to the modelled flux to determine the scaling constant K, which minimises the error between the measured Φ_{meas} and the modelled Φ_{model} flux in the sensor in a least-squares sense, as given by Equation 13:

$$\min_{LS} \left\{ \frac{1}{K} \cdot \Phi_{meas} - \Phi_{model} \right\} \tag{13}$$

The five coils were tested for static positional accuracy, following calibration, with previously described methods [9]. The sensor coils were placed z-directed on the 49-points grid shown in Figure 7, at fixed heights of 85.6 and 152 mm above the field generator, for a total of 98 points. In general, it can be expected that points further from the centre-point of the transmitting board will give rise to the largest errors in position accuracy.

IV. RESULTS

A. Characterisation over frequency

The procedure described in subsection III-B was used to identify all the parameters of Equation 11, given the experimental data. The resulting sensitivity k_s of each coil is reported in Table II, which compares the measured sensitivities to the ones predicted by Equation 10.

For Coil A, Figure 8 shows that the mathematical model accurately predicts the behaviour of the sensor over the frequency. The overshoot at the SRF is higher in the fitted curve

Coil	measurement	formula ($k_s = 2\pi N A_c$)	Error
A	0.18189	0.18323	0.74%
B	0.24678	0.25051	1.51%
C	0.070496	0.06691	-5.08%
D	0.10904	0.11188	2.60%
E	0.23103	0.22839	-1.14%

TABLE II
COMPARISON BETWEEN THE EXPERIMENTAL SENSITIVITY $\boldsymbol{k_s}$ AND THAT PREDICTED BY EQUATION 10.
SENSITIVITY VALUES ARE IN $\mathbf{V\,T^{-1}\,Hz^{-1}}$.

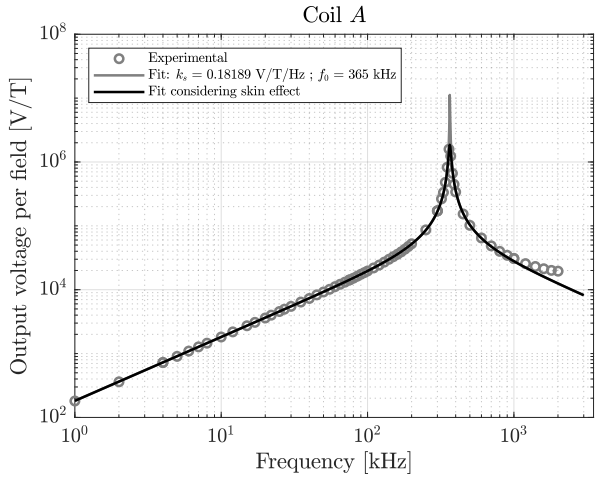

Fig. 8. Measured gain of Coil $\boldsymbol{A}$ over frequency, fit using Equation 11 and corrected fit considering an increased value for the resistance $\boldsymbol{R}$, due to skin and proximity effects.

than in the experimental data, because the resistance used in the model was measured in DC, but at higher frequency its value is bigger, due to skin and proximity effects. Figure 8 shows also the fit where correction for high-frequency effects was considered. Similar results were obtained for the other coils.

The behaviours of the coils over frequency are compared using the curves obtained by the fitting. Figure 9 shows Coils A and B, with almost the same number of turns, N, but different areas. Considering Coil A as a reference, Coil B (larger area) has an increased sensitivity k_s. The SRF f_0 is higher for Coil B due to a smaller value of parasitic capacitance, since L is not smaller, as stated in Table I.

Figure 10 shows Coils A, C, D and E, where the turns N (refer to Table I) are changed. In this case, increasing N, the sensitivity k_s increases and the SRF decreases, due to a larger value of L.

Figure 11 compares the behaviour of Coil B before and after the insertion of a ferrite core. The effects are a lower SRF and an increment of the sensitivity of around 10 dB. This provides an indirect measurement of the apparent permeability, which results $\mu_a = 2.73$.

The apparent magnetic permeability μ_a of the ferrite core was experimentally measured using a combination of the Helmholtz coil configuration used to generate the applied field (the same used for the characterisation of subsection III-B) and a handheld commercial gaussmeter (*GM07* from *Hirst*

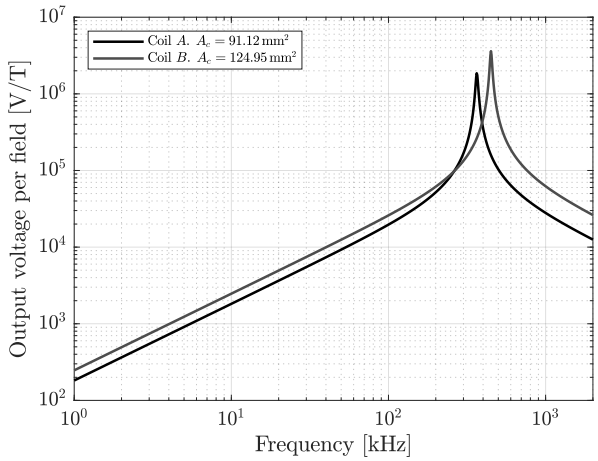

Fig. 9. Behaviours of Coils $\boldsymbol{A}$ and $\boldsymbol{B}$ over frequency. Varying parameter: $\boldsymbol{A_c}$.

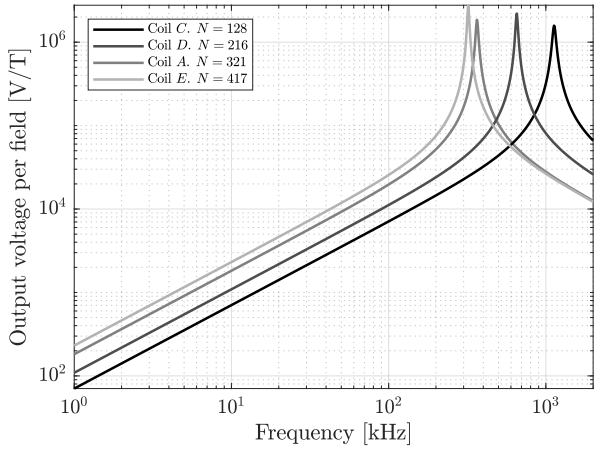

Fig. 10. Behaviours of Coils $\boldsymbol{C}$, $\boldsymbol{D}$, $\boldsymbol{A}$ and $\boldsymbol{E}$ over frequency. Varying parameter: $\boldsymbol{N}$.

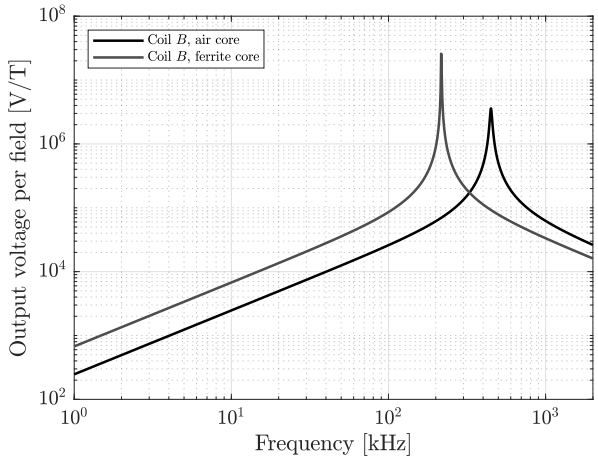

Fig. 11. Behaviour of Coil $\boldsymbol{B}$ with air and ferrite core. Varying parameter: $\boldsymbol{\mu_a}$.

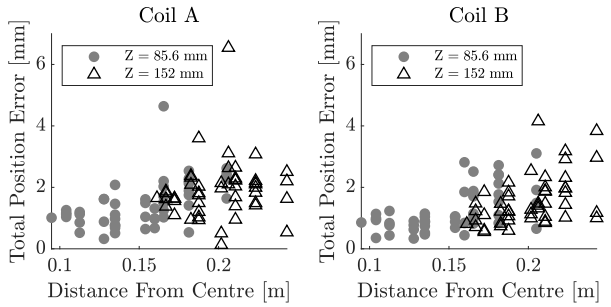

Fig. 12. Error plots for Coils *A* and *B*.

Magnetic Instruments Limited, Falmouth, UK) which was used to measure the average flux density at various points on the core's surface. These investigations yielded an average apparent magnetic permeability of 2.72. It should be noted that this experimental value is significantly less than that predicted by theoretical methods [12] [16], although the differences are accounted by the effects of machining of the ferrite core prior to use resulting in increased demagnetisation effects.

B. Static Accuracy Testing

Static accuracy was determined by calculating the standard deviation between the reported sensor positions and the absolute positions of the sensor above the field generator, *i.e.* the expected values. Equation 14, reported for σ_x but evaluated similarly for σ_y and σ_z, was used to calculate the volume-averaged RMS error along each axis:

$$\Delta x^i = |x^i_{meas} - x^i_{ref}|\,; \qquad \sigma_x = \sqrt{\frac{1}{P}\sum_{i=1}^{P}(\Delta x^i)^2} \tag{14}$$

where x^i_{meas} is the measured x position, x^i_{ref} is the absolute x coordinate of the i^{th} point and $P = 98$ is the total number of test-points. The volume-averaged total RMS error (E_{RMS}) was obtained by vector addition of the standard deviation in each direction (Equation 15), equivalent to the standard deviation of the total distance between measured and reference positions at each experimental point (Equation 16), considering null the expected value of the error:

$$E_{RMS} = \sqrt{\sigma_x^2 + \sigma_y^2 + \sigma_z^2} = \sqrt{\frac{1}{P}\sum_{i=1}^{P}(r^i)^2} \tag{15}$$

where r^i is the total error made at point i, in the sense of distance:

$$r^i = \sqrt{(\Delta x^i)^2 + (\Delta y^i)^2 + (\Delta z^i)^2} \tag{16}$$

Figure 12 shows the total position error at each point r^i as a function of distance from the origin of the field generator, for Coils A and B. Each coil has approximately equal turn count as noted in Table I and these coils were used to investigate the effect of increasing A_c on positional accuracy. No ferrite cores were used with Coils A or B.

Figure 13 shows the total position error r^i for Coils C, D and E, in the absence of any ferrite core. In this case, each

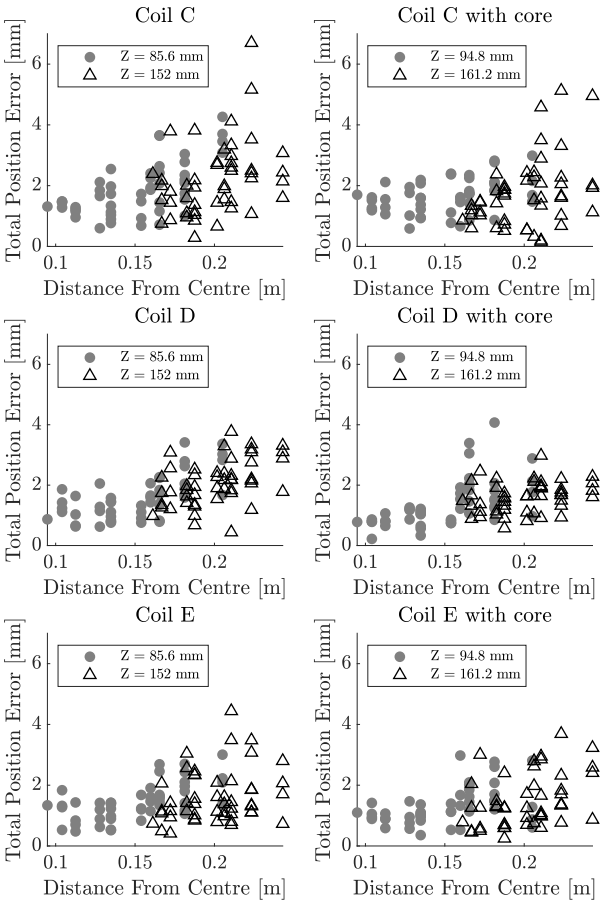

Fig. 13. Error plots for Coils *C*, *D* and *E* with and without ferrite cores.

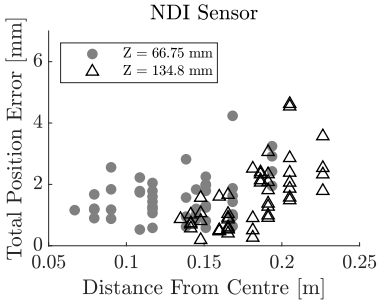

Fig. 14. Error plots for the NDI coil.

coil has approximately equal core area A_c and the aim was to investigate the effect of increasing N on positional accuracy, in the absence of ferrite cores.

Static position errors are summarized in Table III, which includes sensitivity measurements k_s. It can be observed that an increase of k_s is related to an increased tracking accuracy. Figure 15 shows the plot of the total RMS error E_{RMS} of each coil versus k_s. The dataset is too small to demonstrate correlation, but coil sensitivity is clearly an important parameter which affects the static positioning accuracy, as might be expected.

Figure 13 also shows the effect of inserting the 4.5 mm 3C90 ferrite core, described in section III-A, into Coils C, D and E. For comparison, a commercial NDI sensor with

Coil	$k_s \left[\frac{\mathrm{V}}{\mathrm{T\,Hz}}\right]$	σ_x [mm]	σ_y [mm]	σ_z [mm]	E_{RMS} [mm]
A	0.1819	1.05	1.23	0.97	1.89
B	0.2468	0.86	0.99	0.90	1.59
C	0.0705	1.57	1.50	1.52	2.48
D	0.1090	1.14	1.08	1.26	1.98
E	0.2310	0.99	1.09	0.84	1.70

TABLE III
STATIC ACCURACY OBTAINED IN THE TRACKING TEST WITH AIR-CORE COILS.

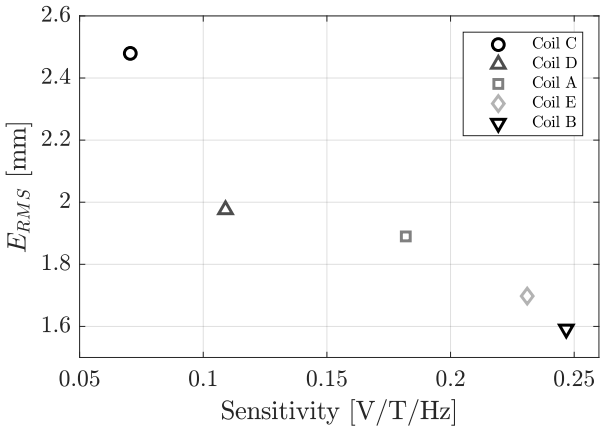

Fig. 15. Relation between static accuracy (total error E_{RMS}) and sensitivity k_s.

ferrite core (part no. 610099, *Northern Digital Inc., Waterloo, Canada*) was also tested for static accuracy (Figure 14). The results are summarized in Table IV.

The effect of the ferrite core is more clearly demonstrated in the results of Figure 16, which shows the Fast Fourier Transform (FFT) of the sensor voltage at a fixed position $(x, y, z) = (0, 0, 85)\,\mathrm{mm}$ from the field generator. Each voltage peak corresponds to the induced voltage due to one of the eight transmitting coils. The plot shows that the ferrite core increases the sensor voltage by approximately 10 dB for the four transmitting coils located closest to the origin of the field generator.

V. DISCUSSION

The coils presented in this work are limited to geometries which were practical for hand-winding without automation. Significantly smaller coils capable of 5 DoF and 6 DoF sensing could be achieved with automated coil winding. However, the resultant coil geometries provided excellent inductive

Coil	N	σ_x [mm]	σ_y [mm]	σ_z [mm]	E_{RMS} [mm]
C	120	1.04	0.89	1.31	1.90
D	216	1.13	0.73	0.91	1.62
E	417	0.86	1.04	0.81	1.58
NDI	/	1.19	1.12	0.73	1.79

TABLE IV
STATIC ACCURACY OF COILS C, D AND E, WITH FERRITE CORES. COMPARISON WITH THE NDI SENSOR.

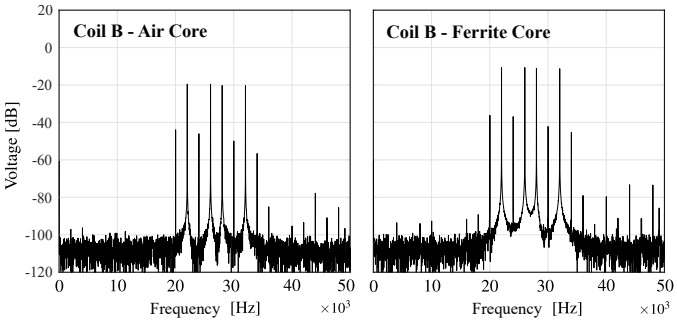

Fig. 16. Fast Fourier Transform of the sensed voltage in Coil B with air and ferrite cores. Voltage units are in decibels (dB) with respect to 1 V.

properties over the frequency range of the Anser EMT system. The voltage gain was approximately tripled (+10 dB) using the ferrite core, as shown in Figure 16. Referring to Equation 3, this approximately corresponds to an apparent magnetic permeability $\mu_a \approx 3$.

The measurements of sensors sensitivities over frequency demonstrated that the analytical model of Figure 5 is very accurate for an inductive sensor in low frequency. Some differences between the model and the experimental data arise over the SRF, where a Finite Element Analysis would be more representative. However, in our EMT application, the inductive sensor works under its SRF.

This work demonstrated that the main parameter of interest for tracking accuracy is the coil sensitivity k_s. This is to be expected because, as predicted by Equation 9, the sensed voltage v_s is linearly dependent on k_s and so the signal-to-noise ratio increases correspondingly, with a resultant improvement in tracking accuracy. As demonstrated in Table II, k_s can be effectively predicted by Equation 10. Although this is expected, it has never been demonstrated in the context of EMT.

Static accuracy measurements were completed for each air-core coil and, in the case of Coils C, D, and E, the results were compared to the case with the addition of a ferrite core. Sensitivity values and position errors of the coils investigated are reported in Table III.

Coil B explores the effect of increasing the coil area A_c on total tracking error. With respect to Coil A, the incremental increase in sensitivity of Coil B is 35.68 % and the corresponding average positioning error decreases by 35.89 %. Care needs to be taken in the numerical calculation of the expected B field across A_c, to account for spatial variations which can generally be disregarded with small point-based sensors such as the NDI probe included in Table IV.

The effect of turn count N on tracking accuracy was studied. Considering Coil C as a baseline, with $N = 120$ turns and $k_s = 0.0705\,\mathrm{V\,T^{-1}\,Hz^{-1}}$, Coils D, A and E have a larger number of turns, yielding increased sensitivities by 54.61 %, 158 % and 228 %. Consequently, the static tracking accuracy improves by 20.16 %, 23.79 % and 31.45 % respectively, in terms of total RMS error. It should be noted that N also increases the value of the inductance and parasitic capacitances, lowering the bandwidth of the sensor. Moreover, a longer winding wire has a larger resistance and this increases the

thermal noise, lowering the signal-to-noise ratio.

In summary, we can observe that the sensitivity and tracking accuracy have a strong linear correlation with coil area as well as with turn count. Overall, the relation between the total static tracking error (Equation 15) and the sensor sensitivity (Equation 10) seems to be strict, as indicated by Figure 15.

The addition of a magnetic core to Coils C, D and E improves tracking accuracy in the case of all three coils. The comparison between Table III and Table IV shows a reduction in the total RMS error of $0.58\,\mathrm{mm}$, $0.36\,\mathrm{mm}$ and $0.12\,\mathrm{mm}$ or $23.4\,\%$, $18.2\,\%$ and $7.1\,\%$ for Coils C, D and E respectively, in the presence of the ferrite core. However, a magnetic core can introduce non-linearities and occupies the inner space of the coil, so it is not compatible with some applications where a coil is winded around the instrument to be tracked.

Finally, it has to be noted that the large-area coils presented in this work can resolve the position with errors significantly smaller (less than $2\,\mathrm{mm}$) than their diameter (about $10\,\mathrm{mm}$), where the resolved position corresponds to the coil geometric centre. For example, the total RMS error of the NDI coil — found here as $1.85\,\mathrm{mm}$ but previously reported as 0.8 mm [17] — is bigger than its diameter, of $0.5\,\mathrm{mm}$. This means that the sensor dimension does not affect the position accuracy, as long as the point-based approximation used in Equation 3 is valid or the spatial integration of the magnetic field across the coil cross-section (see Equation 8) is performed.

VI. Conclusions

This work represents the first investigation of bespoke sensor designs for medical applications of electromagnetic tracking with reported RMS errors between $1.58\,\mathrm{mm}$ and $2.48\,\mathrm{mm}$. As predicted, errors are decreased by the use of sensors with increased sensitivities; larger diameter coils, additional winding turns and the presence of a ferrite core. The devices used to validate the proposed prototype inductive sensors were limited to tracking of large laparoscopic and endoscopic instruments. However, the principles and experimental results indicate that the approach of this paper can be easily used to produce highly-integrated sensors for instrument tracking, with an excellent prediction of sensor sensitivity based on simple theoretical calculations.

References

[1] J. P. Díaz-Jimenez and A. N. Rodriguez, "Interventions in pulmonary medicine," in *Interventions in Pulmonary Medicine*, J. P. Díaz-Jimenez and A. N. Rodriguez, Eds. Springer International Publishing, pp. 1–645.

[2] K. A. Khan, P. Nardelli, A. Jaeger, C. O'Shea, P. Cantillon-Murphy, and M. P. Kennedy, "Navigational Bronchoscopy for Early Lung Cancer: A Road to Therapy," vol. 33, no. 4, pp. 580–596.

[3] E. J. Hermann, H.-H. Capelle, C. A. Tschan, and J. K. Krauss, "Electromagnetic-guided neuronavigation for safe placement of intraventricular catheters in pediatric neurosurgery," vol. 10, no. 4, pp. 327–333.

[4] F. Kral, E. J. Puschban, H. Riechelmann, F. Pedross, and W. Freysinger, "Optical and electromagnetic tracking for navigated surgery of the sinuses and frontal skull base."

[5] E. E. Folch, M. R. Bowling, T. R. Gildea, K. L. Hood, S. D. Murgu, E. M. Toloza, M. M. Wahidi, T. Williams, and S. J. Khandhar, "Design of a prospective, multicenter, global, cohort study of electromagnetic navigation bronchoscopy," vol. 16, no. 1, p. 60.

[6] D. H. Yu and D. Feller-Kopman, "Interventional bronchoscopy in adults," vol. 12, no. 3, pp. 239–248.

[7] K. Lam, J.-L. Bigcas, A. Luong, W. Yao, and M. J. Citardi, "Flexible Microsensor Technology for Real-Time Navigation Tracking in Balloon Sinus Ostial Dilation," vol. 8, no. 1, p. ar.2017.8.0193.

[8] OpenEMT. [Online]. Available: https://openemt.org

[9] H. A. Jaeger, A. M. Franz, K. O'Donoghue, A. Seitel, F. Trauzettel, L. Maier-Hein, and P. Cantillon-Murphy, "Anser EMT: The first open-source electromagnetic tracking platform for image-guided interventions."

[10] H. Mansfield, P. Cantillon-Murphy, J. Griffiths, D. Eustace, M. O'Shea, K. O'Donoghue, and T. Power, "Catheter Position Tracking System Using Planar Magnetics and Closed Loop Current Control," vol. 50, no. 7, pp. 1–9.

[11] C. Coillot and P. Leroy, "Induction Magnetometers Principle, Modeling and Ways of Improvement," in *Magnetic Sensors - Principles and Applications*, K. Kuang, Ed. InTech, ch. 3.

[12] S. Tumanski, "Induction coil sensors - A review."

[13] K. O'Donoghue, "Electromagnetic tracking and steering for catheter navigation." [Online]. Available: https://cora.ucc.ie/handle/10468/2025

[14] P. Ripka, *Magnetic Sensors and Magnetometers*, vol. 13.

[15] M. Zahn, "The magnetic field," in *RES.6-002 Electromagnetic Field Theory: A Problem Solving Approach*, spring ed. Massachusetts Institute of Technology: MIT OpenCourseWare, ch. 5, pp. 313–392. [Online]. Available: https://ocw.mit.edu

[16] B. K. Pugh, D. P. Kramer, and C. H. Chen, "Demagnetizing factors for various geometries precisely determined using 3-D electromagnetic field simulation," vol. 47, no. 10, pp. 4100–4103.

[17] L. Maier-Hein, A. M. Franz, W. Birkfellner, J. Hummel, I. Gergel, I. Wegner, and H. P. Meinzer, "Standardized assessment of new electromagnetic field generators in an interventional radiology setting," vol. 39, no. 6, pp. 3424–3434.

Marco Cavaliere (M'20) received the *Laurea* in Energy Engineering and the *Laurea Magistrale* in Electrical Energy Engineering from the University of Padua, Italy, in 2017 and 2019 respectively. He is currently pursuing the Ph.D. degree in Electrical and Electronic Engineering with University College Cork and Tyndall National Institute, Cork, Ireland. His current research interests include electromagnetic tracking and navigation systems for image-guided interventions.

Oisín McVeigh is currently pursuing a B.E. degree in Electrical and Electronic Engineering from University College Cork, Ireland.

Herman Alexander Jaeger (S'18–M'19) received B.E., M.Eng.Sc. and Ph.D. degrees in Electrical and Electronic Engineering from University College Cork, Ireland, in 2014, 2015 and 2018 respectively. He is currently a Post-Doctoral Researcher with UCC. His current interests include electromagnetic tracking and navigation for image-guided interventions.

Stephen Hinds received B.Sc. and M.Eng.Sc. degrees in Computer Science from University College Cork, Ireland. His research interests include investigating the role of electromagnetism in image-guided interventions and developing software for open-source electromagnetic tracking systems and AR/VR applications.

Kilian O'Donoghue received B.E. and Ph.D. degrees in Electrical and Electronic Engineering from University College Cork, Ireland, in 2011 and 2015 respectively. His research interests include EM tracking systems, circuit design, magnetic field modelling and minimally invasive surgeries.

Pádraig Cantillon-Murphy is Senior Lecturer in Electrical and Electronic Engineering at University College Cork, Ireland, Academic Member of Tyndall National Institute at University College Cork, and an honorary faculty at l'Institut de Chirurgie Guidée par l'Image in Strasbourg. He received B.E. degree (2003) from UCC, before completing his M.Eng.Sc. (2005) and Ph.D. (2008) degrees at the Department of Electrical Engineering and Computer Science at Massachusetts Institute of Technology (MIT). He is Principal Investigator at the Biomedical Design Laboratory at UCC and Tyndall National Institute which explores novel device development in image-guided surgery and endoscopy. His current research interests include magnets for surgery, electromagnetic tracking and navigation and surgical robotics.